

Thesis Title

A subtitle of your thesis

Author name



Thesis submitted for the degree of
Master in Master's Program Name <change at
main.tex>
60 credits

Department Name <change at main.tex>
Faculty name <change in duoforside.tex>

UNIVERSITY OF OSLO

Spring 2022

Thesis Title

A subtitle of your thesis

Author name

© 2022 Author name

Thesis Title

<http://www.duo.uio.no/>

Printed: Reprosentralen, University of Oslo

Abstract

Contents

1	Introduction	1
I	Theory	3
2	High-Entropy alloys	4
2.1	Fundamentals	4
2.2	Core effects and properties	7
3	Modeling of random alloys	9
3.1	The Special Quasi-random Structure model	9
3.1.1	Mathematical description	10
3.1.2	Applications to high-entropy alloys	12
4	Density Functional Theory	16
4.1	Review of Quantum Mechanics	17
4.1.1	The Shrödinger equation	17
4.1.2	Approximations to the many-body Shrödinger equation	18
4.2	Kohn-Sham density functional theory	20
4.2.1	Density functional theory	20
4.2.2	The Kohn-Sham Equation	21
4.3	Limitations of DFT	22
II	Method	24
5	Practical aspects of DFT	25
5.1	The Exchange-Correlation functional	25
5.1.1	Local density approximation	25
5.1.2	Generalized gradient approximation	26
5.1.3	Meta-GGA	26
5.1.4	Hybrid functionals	27
5.1.5	Outlook	27
5.2	Plane waves and reciprocal space	28
5.3	Self-consistent field calculation	30

6	Computational details	32
6.1	Vienna Ab initio Simulation Package	32
6.2	Material	34
6.3	Work flow and dependencies	35
III	Results and Discussion	37
7	(CrFeMnNi)Si₂ in the β-FeSi₂ structure	39
7.1	Bulk β -FeSi ₂	39
7.2	(CrFeMnNi)Si ₂ SQSs	40
7.2.1	The band gap	42
7.2.2	Local and projected density of states	45
7.2.3	The band gap with SCAN and HSE06	47
7.2.4	Pair distribution functions	52
7.2.5	SQS size	54
8	Different compositions	58
8.1	Exploring the quaternary phasidiagram	58
8.2	Replacing elements	63
10	Overview and outlook	65
10.1	Literature	65
10.2	General thoughts	66
10.3	Other things	70
10.4	Cr ₄ Fe ₄ Mn ₄ Ni ₄ Si ₃₂ in different crystal structures	73
10.5	Overview	75
IV	Conclusion	76
A	Compositions	73
A.1	Projected density of states	73
A.2	Probability distribution functions	76
B	Eqvimolar alloy	78
B.1	DOS	78
C	Charge density	80

List of Figures

2.1	Formation of HEA based on δ and N . Figures adopted from [2]	6
2.2	A schematic illustration of lattice distortion in high-entropy alloys. Figure from [5]	8
3.1	PDFs of (a) 20 and (b) 250 atom SQS models of CrFeMnNi [12]	13
3.2	Density of states with SQS and MC/MD of FCC CoCrFeNi, figure from [12]	14
3.3	Probability distribution functions with SQS and MC/MD of HCP CoOsReRu [12]	14
4.1	Number of DFT studies per year from 1980 to 2021 [20]. . . .	16
5.1	Calculated to experimental band gap measurements of Becke-Johnson, modified Becke-Johnson and SCAN functionals [35]	27
5.2	Self consistent iteration of a DFT calculation. Figure adopted from lecture notes fys-mena4111 [18]	30
6.1	48 atom SQS based on eqvimolar distribution of Cr, Fe, Mn and Ni in and $FeSi_2$ cell.	36
7.1	Density of states (PBE) β - $FeSi_2$	39
7.2	Density of states of SQS D (CrFeMnNi) Si_2 with PBE.	42
7.3	Density of states of SQS B (CrFeMnNi) Si_2 with PBE.	42
7.4	Local density of states of Si (SQS D)	45
7.5	Local density of states of (a) Cr, (b) Mn, (c) Fe, (d) Ni in SQS D.	45
7.6	Projected density of states SQS D CFMN (fesi2) from PBE calculation	46
7.7	Projected density of states of SQS D and B around E_F	46
7.8	Density of states illustrating the band gaps from PBE and SCAN calculations for SQS E and D.	48
7.9	Density of states of SQS B with HSE06	48
7.10	Probability distribution function of SQS D (top) and B (bottom)	52
7.11	CPU time, Make log plot instead	54
7.12	Density of states of SQS E 192 atom SQS.	56
7.13	Pair distribution functions of SQS sizes (top) 48 atoms, (middle) 96 atoms, (bottom) 192 atoms	57

8.1	Projected density of states of (a) $\text{Cr}_3\text{Fe}_3\text{Mn}_7\text{Ni}_3\text{Si}_{32}$ (SQS B), (b) $\text{Cr}_5\text{Fe}_5\text{Mn}_3\text{Ni}_3\text{Si}_{32}$ (SQS C), (c) $\text{Cr}_5\text{Fe}_3\text{Mn}_5\text{Ni}_3\text{Si}_{32}$ (SQS A), (d) $\text{Cr}_3\text{Fe}_5\text{Mn}_5\text{Ni}_3\text{Si}_{32}$ (SQS D)	61
8.2	Projected density of states of $\text{Cr}_3\text{Fe}_3\text{Mn}_3\text{Ni}_7\text{Si}_{32}$ around E_F .	62
8.3	Projected density of states of $(\text{CrFeMnCo})\text{Si}_2$	65
8.4	Density of states of a) $(\text{CrFeCoNi})\text{Si}_2$ and b) $(\text{CrFeTiNi})\text{Si}_2$. .	66
8.5	Density of states of two SQSs of $(\text{CoFeMnNi})\text{Si}_2$	66
A.1	ch $\text{Cr}_4\text{Fe}_4\text{Co}_4\text{Ni}_4\text{Si}_{32}$	73
A.2	ch $\text{Co}_4\text{Fe}_4\text{Mn}_4\text{Ni}_4\text{Si}_{32}$	74
A.3	ch $\text{Cr}_4\text{Fe}_4\text{Mn}_4\text{Co}_4\text{Si}_{32}$	74
A.4	ch $\text{Cr}_4\text{Fe}_4\text{Ti}_4\text{Ni}_4\text{Si}_{32}$	75
A.5	ch $\text{Cr}_4\text{Fe}_4\text{Mn}_4\text{Ti}_4\text{Si}_{32}$	75
A.6	Probability distribution functions of top: $\text{Co}_4\text{Fe}_4\text{Mn}_4\text{Ni}_4\text{Si}_{32}$ (SQS D), middle: $\text{Cr}_4\text{Fe}_4\text{Co}_4\text{Ni}_4\text{Si}_{32}$ (SQS B), bottom: $\text{Cr}_4\text{Fe}_4\text{Mn}_4\text{Co}_4\text{Si}_{32}$ (SQS B)	76
A.7	Probability distribution function of top: $\text{Cr}_4\text{Fe}_4\text{Mn}_4\text{Ti}_4\text{Si}_{32}$ (SQS B), bottom: $\text{Cr}_4\text{Fe}_4\text{Ti}_4\text{Ni}_4\text{Si}_{32}$ (SQS B))	77
B.1	Density of states SQS A $(\text{CrFeMnNi})\text{Si}_2$ with PBE.	78
B.2	Density of states SQS E $(\text{CrFeMnNi})\text{Si}_2$ with PBE.	79

List of Tables

7.1	Total energy per atom, final magnetic moment and band gap of 5 unique SQS of (CrFeMnNi)Si ₂ based on the β -FeSi ₂ unit cell.	40
7.2	Band gap of the 5 SQSs of (CrFeMnNi)Si ₂ calculated from the eigenvalues in spin up, down and total.	43
7.3	Band gap of SQS D as a function of occupancy in the eigenvalues.	44
7.4	Band gap calculated with PBE, SCAN and HSE06 XC-functionals of (CrFeMnNi)Si ₂ SQSs.	47
7.5	Minimum gap between k-point in valence band and conduction band in SQS B from PBE, SCAN and HSE06	49
7.6	Band gap from HSE06 calculations with gaussian smearing and smearing width <i>sigma</i> equal to 0.05 and 0.005, and the tetrahedron method (TBC). "-" mean unchanged values, "ND" means not done.	50
7.7	Overview 48, 96 and 192 SQSs.	54
7.8	Band gap of SQSs of 48, 96 and 192 atoms each of (CrFeMnNi)Si ₂ . The names are arbitrary, ie A in 48 does not equal A in 96 or 192.	55
8.1	Summary composition diagram	58
8.2	Band gaps of various compositions of (CrFeMnNi)Si ₂ . Most stable SQS of a set is highlighted in bold text, defect band gap are listed in cursive. Some SQSs were excluded from the table due to unsuccessful calculations.	60
8.3	Overview new compositions	63
8.4	Final magnetic moment of the most stable supercell of each composition.	64
8.5	Band gaps of the most stable SQS of β -FeSi ₂ high-entropy silicide compositions as a function of occupancy in the eigenvalues.	65
10.1	Mean and standard deviation of the total energy and magnetic moment per atom, plus enthalpy of formation of the listed mean energies (FeSi ₂).	68

10.2 Total and spin dependent band gap of 4 permutations of CFMN (fesi2) with PBE GGA calculation. The structures that are excluded from this list either failed in calculations, or does not show any band gap.<	70
---	----

Preface

Chapter 1

Introduction

some introduction on the importance of discovering new materials and alloying.

Need something on thermoelectricity related to both the band gap and high-entropy alloys.

High-entropy alloys is a novel class of materials based on alloying multiple components, as opposed to the more traditional binary alloys. This results in an unprecedented opportunity for discovery of new materials with a superior degree of tuning for specific properties and applications. Recent research on high-entropy alloys have resulted in materials with exceedingly strong mechanical properties such as strength, corrosion and temperature resistance, etc **find references**. Meanwhile, the functional properties of high-entropy alloys is vastly unexplored. In this study, we attempt to broaden the knowledge of this field, the precise formulation of this thesis would be an exploration on the possibilities of semiconducting high-entropy alloys.

A key motivation of this thesis is the ability to perform such a broad study of complex materials in light of the advances in material informatics and computational methods. In this project, we will employ Ab initio methods backed by density functional theory on top-of the line supercomputers and software. 20 years ago, at the breaking point of these methods, this study would have been significantly narrower and less detailed firstly, but secondly would have totaled ... amount of CPU hours to complete (**Calculate this number**). In the addition to the development in computational power, is also the progress of modeling materials, specifically we will apply a method called Special Quasi-random Structures (SQS) to model high-entropy alloys or generally computationally complex structures. Together with the open landscape of high-entropy alloys described above, these factors produce a relevant study in the direction of applying modern computational methods to progress the research of a novel material class and point to promising directions for future research.

In specifics, this thesis revolve around the electrical properties of high-entropy alloys, mainly the band gap as this is the key indicator for a semiconducting material and it's applicability. Semiconductors are the building blocks in many different applications in today's world, ranging

from optical and electrical devices, to renewable energy sources such as solar and thermoelectricity. Given the economic and sustainable factors concerning silicon, in addition to its role in relevant applications such as microelectronics and solar power. Silicon emerges as a natural selection to build our alloys around. Furthermore, the development and research on both high entropy alloys and metal silicides have been heavily centered around 3d transition metals. Keeping in line with the economic and environmental factors, we will continue this direction by focusing on high entropy stabilized sustainable and economic 3d metal silicides **Not happy with this writing**. Throughout the study we will analyze a great number of permutations of 3d silicides, from different initial metal silicides such as $CrSi_2$, $FeSi_2$, $MnSi_{1.75}$, Fe_2Si , each with distinct properties relating to the band gap, crystal structure and metal to silicon ratio. In addition, the permutations include numerous metal distributions and elements within the 3d-group of metals. Examples are Co, Cr, Fe, Mn, and Ni.

Given a background in high-entropy alloys, one could ask if this study is truly sensible. In the later sections we will cover the details of this field, and it quickly become clear that the materials investigated in this study does not fall under the precise definition of high-entropy alloys, nor do we intend to explore the properties and factors relating to high-entropy stabilized alloys such as the configurational entropy, phase stability and finite temperature studies. However this study is motivated from the discovery of these materials and promising properties, and venture into a more hypothetical space of materials, enabled by the computational methods available to study the potential properties of such materials. On the other hand, very recent studies **Mari, and other HEA silicide study** have experimentally synthesized high-entropy disilicides, thus in some way justifying the direction of this project.

We begin this project by reviewing key concepts of solid-state physics for readers lacking a background in materials science, and an introduction to the base 3d silicides of the experimental work. Later follows a theoretic walk-through of the relevant concepts of this thesis, these topics include high-entropy alloys, special quasi-random structures, and density functional theory. Next we shine light on the implementation of DFT in this project, and other computational details required to reproduce the results in this thesis, such as the use of the Vienna Ab Initio Simulation Package (VASP) and implementation of SQS. Finally we present the results of our study, these include the band gap and electronic properties of various structures and the success and challenges of the computational methods applied throughout the study.

Part I

Theory

Chapter 2

High-Entropy alloys

High-Entropy Alloys have become a quickly emerging field in materials science in part to the increased flexibility and possibilities in discovering new materials with unique properties. Since the original discovery in 2004, as of 2015 there have been over 1000 published journal articles on high-entropy alloys. In the following section we introduce the fundamentals and some of the applications of high-entropy alloys, this section will be based on the fantastic description of HEAs in "High-Entropy Alloys - Fundamentals and Application", in particular chapters 1,2,3 and 7 [1], [2], [3], [4] and references therein.

2.1 Fundamentals

A high entropy alloy can be compared to a smoothie. In a smoothie one can produce unique combinations of flavors and nutritional values based on both the properties of the distinct fruits and vegetables, and their interplay in the mixture. In materials science, this exact procedure can be applied to generate a large range of materials with tunable properties depending on the intended application. In respect to HEA's, examples are increased strength, ductility, corrosive resistance or lowered thermal conductivity. Moving on from the rather banal fruit analogy, a high-entropy alloy can be defined typically falls under the two conditions.

1. The material consist of at least 5 distinct elements, where each element contribute between 5-35% of the composition
2. The total configurational entropy is greater than $1.5R$, where R is the gas constant.

The latter is an especial case for high-entropy alloys. The ideal configurational entropy of random N -component solid-solution is given in eq 2.1

$$\Delta S_{\text{config}} = -R \sum_{i=1}^N X_i \ln X_i, \quad (2.1)$$

it's clear that ΔS_{config} increase with a higher number of constituents in the mix. For instance, the ideal configurational entropy of a binary alloy

is $0.69R$, while a 5-component alloy is $1.61R$. If we neglect other factors that influence the formation of solid solutions (will be covered later), from Gibbs free energy in eq 2.2

$$\Delta G_{\text{mix}} = \Delta H_{\text{mix}} - T\Delta S_{\text{mix}}, \quad (2.2)$$

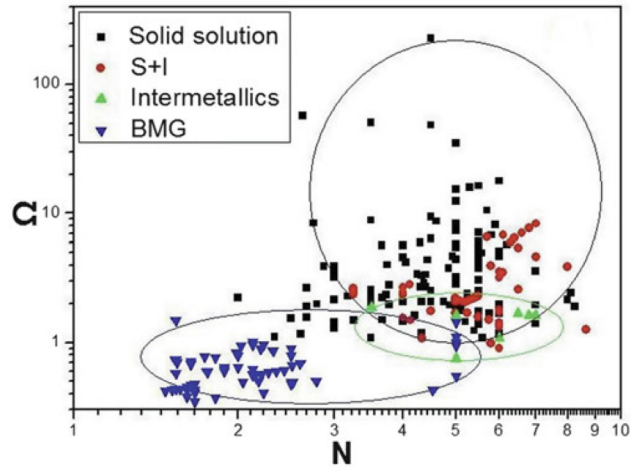
the two primary factors in formation of solid solution is the mixing enthalpy, which is the driving force to form compounds, and the mixing entropy which is the driving force to form random solid solutions. At elevated temperatures especially, the energy associated to the entropy of the system becomes comparative to the mixing enthalpy and can impact the overall equation. In summary, the overall concept of high-entropy alloys is that through alloying a greater number of elements, the gain in configurational entropy of the system prohibit the formation of intermetallic compounds in favor of a random solid solution. The random term simply relate to the various components occupying lattice positions based on probability. In fact, a narrower definition of high-entropy alloys would be structures with a single-phase disordered solid solution. The two "definitions" given previously can be considered as guidelines for the latter.

All though the mixing entropy mentioned above plays a central role in the formation, there are other factors to consider, and some that may oppose the formation of a single disordered phase. One of these is the atomic size effect which is related to the differences in atomic size, between the various elements in the alloy, this quantity is denoted δ . Y. Zhang et al. in 2008 illustrated the relationship between ΔH_{mix} and δ . When δ is very small, ie similar atomic sizes. The elements have an equal probability to occupy lattice sites to form solid solutions, but the mixing enthalpy is not negative enough to promote formation of solid solution. Increasing δ does result in greater ΔH_{mix} , but leads to a higher degree of ordering. **Include figure?** To summarize the illustration, the formation of solid solution high-entropy alloys occur in a narrow range of δ value that satisfy both the enthalpy of mixing and the disordered state. Recently, Yang and Zhang proposed the parameter Ω to evaluate the stability of high-entropy alloys. The quantity is a product of the melting temperature T_m , mixing entropy and mixing enthalpy in the following manner

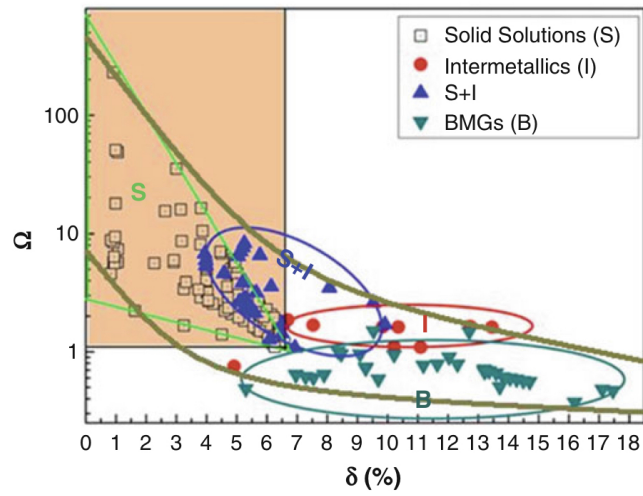
$$\Omega = \frac{T_m \delta S_{\text{mix}}}{|\Delta H_{\text{mix}}|}. \quad (2.3)$$

They managed to obtain a qualitative condition for formation of the single disordered solid solution at $\Omega \geq 1.1$ and $\delta \leq 6.6\%$. While compounds such as intermetallics form for greater values of δ and lesser values of Ω . Similarly, replacing the atomic size effect constant for the number of elements result in an equivalent condition. The results are summarized in figure 2.1

An important quantity in terms of characterizing high-entropy alloys is the total number of electrons VEC. The valence electron concentration of a material is strongly related to the crystal structure of the material. For example, Co_3V , originally a hexagonal structure can be transformed into



(a) HEA formation based on Ω and δ



(b) HEA formation based on Ω and N

Figure 2.1: Formation of HEA based on δ and N . Figures adopted from [2]

a tetragonal or cubic structure by either increasing the VEC from alloying with Ni, or reduction with Fe respectfully. Derived from the work of Guo et al. on the phase stability of a $Al_xCrCuFeNi_2$ HEA, the VEC can be directly related to the crystal structure of high-entropy alloys. A lower VEC stabilize the BCC phase, while higher values stabilize FCC. In between is a mixture of the two. Specifically values greater than 8.0 stabilize FCC, and values below 6.87 favor BCC. However, these boundaries are not rigid when including elements outside of transition metals, exceptions have also been found for high-entropy alloys containing *Mn*. All though a heavy majority of reported high-entropy alloys that form solid solutions have been found to adopt simple cubic structures such as FCC and BCC. Recent studies have observed HEA's in orthorhombic structures like $Ti_{35}Zr_{27.5}Hf_{27.5}Ta_5Nb_5$ and hcp structures, for example *CoFeNiTi*.

2.2 Core effects and properties

Next, we will summarize the discussion above into four core effects of high entropy alloys coupled with the unique properties observed in HEAs. The first of these is called the "high-entropy effect", as explained in the previous section the configurational entropy of HEAs is much greater than in traditional solids or even binary alloys, this quantity is central to stabilize the disordered phase ahead of intermetallic or strongly ordered structures. Thus this effect can result in enhanced strength and ductility. From considerations of Gibbs free energy (Eq. 1), we see that this effect is most prominent at elevated temperatures.

The second effect is the "severe lattice distortion effect" that arises from the fact that every element in a high-entropy structure is surrounded by non-homogeneous elements, thus leading to severe lattice strain and stress. The overall lattice distortion is additionally attributed to the differences in atomic size, bonding energies and crystal structure tendencies between the components. Therefore the total lattice distortion observed in HEA's are significantly greater than that of conventional alloys. This effect mostly affect the strength and conductivity of the material, such that a higher degree of distortion yields greater strength and greatly reduces the electronic and thermal conductivity due to increased electron and phonon scattering. An upside to this is that the scattering and following properties become less temperature dependent given that it originates from the lattice rather than thermal vibrations.

The two remaining effects, "sluggish diffusion" and "cocktail effect" can be summarized swiftly. The first is a direct consequence of the multi-component layout of high-entropy alloys that result in slowed diffusion and phase transformation because of the number of different elements that is demanded in the process. The most notable product from this effect is an increased creep resistance. Lastly we have the cocktail effect, which is identical to the smoothie analogy mentioned previously, in that the resultant characteristics is a combination of both the elements and their interaction. This is possible the most promising concept behind high-

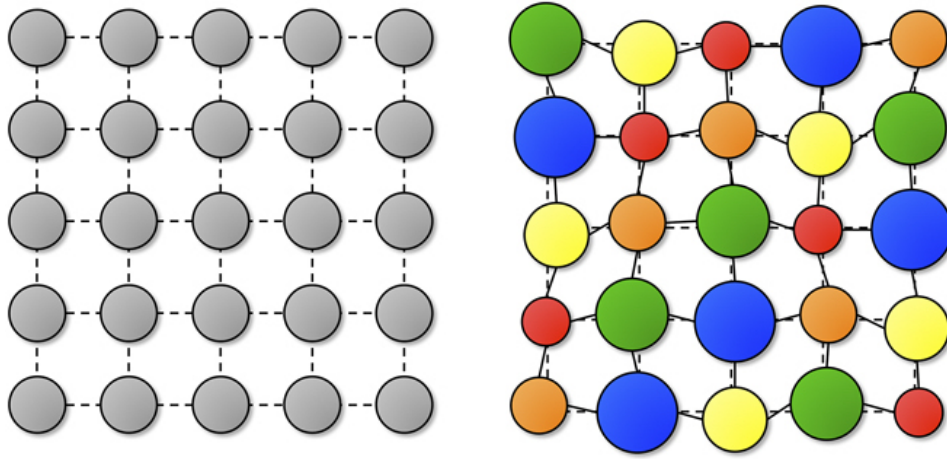


Figure 2.2: A schematic illustration of lattice distortion in high-entropy alloys. Figure from [5]

entropy alloys, which fuels researchers with ambition to discover highly optimized materials by meticulously combining and predicting properties from different elements. Examples of this can be the refractory HEA's developed by "Air Force Research Laboratory" severely exceeding the melting points and strength of previous Ni or Co-based superalloys by alloying specifically refractory elements such as Mo, Nb and W. Another example is the research conducted by Zhang et al. on the high-entropy system $\text{FeCoNi}(\text{AlSi}_x)$ with $(0 < x < 0.8)$. In this HEA it was found that increased amount of either Al or Si lowered the saturation magnetization of the alloy. By tuning the relative amounts, it was found excellent properties for an $x = 0.2$ HEA in terms of the magnetization, electrical resistivity and yield strength to produce a promising soft-magnet. The same was also found in $\text{Al}_{0.2}\text{CoCrFeNi}$ where the larger addition of Ni reduced the ferromagnetism of the alloy and in CoCrCuFeNiTi_x alloys where $x = 0$ was paramagnetic and $x > 0.8$ showed superparamagnetic properties. In general we find that the saturation magnetism is mostly dependent on the contents and distribution of ferromagnetic elements such as Fe, Co and Ni while the addition of anti-ferromagnets like Cr could be difficult to predict. For example addition of Cr to FeCoNi, the ferromagnetic compound becomes paramagnetic.

For example in the ferromagnetic HEA CoFeMnNiX , $X = \text{Al, Cr, Ga, Sn}$, studied in [6], Mn pushed the material to the ferromagnetic phase, meanwhile addition of Cr pushed the material to a paramagnetic phase. Likewise in the equimolar system of CrMnFeCoNi [7], the local magnetic moment of Cr was found to align antiferromagnetic, and the ferromagnetic character was attributed to local magnetic moments of Fe and Mn.

Chapter 3

Modeling of random alloys

The structure of high-entropy alloys in which the alloying elements occupy lattice sites by a random probability pose a problem on the numerical methods used for modeling. DFT in particular rely heavily on the periodicity in crystalline solids, as we will discover later. In a brute force approach, this could be solved by randomly distribute the solute and solvent atoms over the lattice sites of a large supercell and average the energy and related properties of a great number of such supercells with varying distributions. Obviously this approach is very computationally demanding. Today there exists a number of possible methods to more efficiently study such structures. Examples are the virtual crystal approximation (VCA), Coherent Potential approximation (CPA), special quasi-random structure (SQS), and hybrid monte-carlo/molecular dynamics. (MC/MD). A brief review of the different models is given in for example [8]. In this project we will employ the SQS method, due to both it's easy to use implementation and interpretation in VASP compared to the other options, and other benefits that will become clear after the following sections.

3.1 The Special Quasi-random Structure model

In the original paper on SQS published in 1990 [9], it was proposed a selective occupation strategy to design special periodic quasi-random structures that exceeded previous methods in both accuracy and cost. The key concept was to create a periodic unit cell of the various components in a finite N lattice site single configuration such that the structure most closely resemble the configuration average of an infinite perfect random alloy. In an attempt to work withing the 50 lattice sites boundary of ab initio methods at that time, the working theory was that if one can resemble an infinite perfect random alloy by a periodic finite N cell, also the electronic properties would be similar between the two. The solution to this model was that for each N , ie lattice site, to minimize the difference of structural correlation function between the approximated cell and the perfect random alloy. There are obviously errors involved with approximating a random alloy by a periodic cell, but by the hierarchical relation to the properties of

the material, interactions between distant sites only offer a negligible small contribution to the total energy of the system. Thus the aim of the SQS method is focused around optimizing the correlations within the first few shells of a given site. To follow is a review of the mathematical description of the special quasi-random structures method.

3.1.1 Mathematical description

We begin by giving a brief overview over topics such as cluster expansions, statistics and superposition of periodic structures, and present the notation used in the derivation.

The different possible atomic configurations are denoted σ . The physical properties of a given configuration is $E(\sigma)$, and $\langle E \rangle$ is the ensemble average over all configurations. In practice, this quantity is unfeasible in terms of computational cost, seeing as the average require calculations and relaxations of all possible configurations, for a binary alloy this is 2^N for a fixed N number of lattice sites. A solution to this is to use the theory of cluster expansions and discretize each configuration into "figures" f . A figure in the lattice is defined in terms of the number of atoms at each vertex k , the order of neighbor distances separating them m , and position in the lattice l . Further each site in the figure is assigned a spin value \hat{S}_i to denote which element it holds (+1,-1 for a binary alloy). By defining the spin product of spin variables in a figure at lattice position l as $\Pi_f(l, \sigma)$, we can write the average of all locations in the lattice of a given figure f as

$$\Pi_f(\sigma) = \frac{1}{ND_f} \sum_l \Pi_f(l, \sigma), \quad (3.1)$$

where D_f is the number of equivalent figures per site. The brilliance of this notation is that we now can express the physical property $E(\sigma)$ in terms of the individual contributions ϵ_f of a figure f .

$$E(\sigma) = \sum_{f,l} \Pi_f(l, \sigma) \epsilon_f(l) \quad (3.2)$$

The quantity ϵ_f is called the "effective cluster property" and is defined as (for a random binary alloy $A_{1-x}B_x$)

$$\epsilon_f(l) = 2^{-N} \sum_{\sigma} \Pi_f(l, \sigma) E(\sigma) \quad (3.3)$$

Inserting the equation for Π_f into that of $E(\sigma)$ we can describe the the previous cluster expansion of $E(\sigma)$ as

$$E = N \sum_f D_f \langle \Pi_f \rangle \epsilon_f \quad (3.4)$$

Thus we have successfully managed to reduce the expensive task of sampling all $E(\sigma)$ into calculating the effective cluster properties and summing over all types of figures. Remembering that $E(\sigma)$ can relate

to many physical properties, the most common and applied case is that $E(\sigma)$ is the total energy, while ϵ_f is many body interaction energies. The cluster expansion above converge rather quickly with increasing number of figures, an effective method is thus to select a set of configurations to evaluate the effective cluster properties. The next step is to select a finite largest figure denoted F , and "specialize" the cluster expansion to a set of N_s periodic structures $\sigma = s$ to obtain the two expressions for $E(s)$ and ϵ_f using matrix inversion to obtain the result for ϵ_f

$$E(s) = N \sum_f^F D_f \Pi_f(s) \epsilon_f \quad (3.5)$$

$$\epsilon_f = \frac{1}{ND} \sum_s^{N_s} [\Pi_f(s)] - 1E(s) \quad (3.6)$$

Assuming now that the sum of figures F and N_s periodic structures are well converged, $E(\sigma)$ can be rewritten as a superposition of $E(s)$

$$E(\sigma) = \sum_s^{N_s} \zeta_s(\sigma) E(s) \quad (3.7)$$

$$\zeta_s(\sigma) = \sum_f^F [\Pi_f(s)]^{-1} \Pi_f(\sigma) \quad (3.8)$$

where ζ is the weights. Thus we have effectively reduced the problem to a convergence problem of the number of figures F and structures N_s . This can be easily solved given that we are dealing with periodic crystal structures s that can employ the general applications of ordered structures from ab initio methods, and increasing F until the truncation error falls bellow a desired threshold. However, this approach requires that the variance of the observable property is much lower than the sample mean, otherwise one would have to employ a much bigger sample size to reach statistical convergence. Because of the different relationships between various physical properties and the correlation functions, one observe different convergence depending on the meaning of E . The idea behind SQS was therefore to design single special structures with correlation functions $\Pi_f(s)$ that most accurately match those of the ensemble average of a random alloy $\langle \Pi_f \rangle_R$.

The correlation functions of an perfect random infinite alloy, denoted as R is defined bellow

$$\Pi_{k,m}(R) = \langle \Pi_{k,m} \rangle_R = (2x - 1)^l \quad (3.9)$$

with k, m defined as before and x being the composition ratio of the alloy. In the case of an eqvimolar alloy ($x = \frac{1}{2}$), the functions equal 0 for all k except $\langle \Pi_{0,1} \rangle_R = 1$. If we now randomly assign either atom A or B to every lattice site, for a sufficiently large value of N , the goal is then to create a single configuration that best match the random alloy. Keeping with the $x = \frac{1}{2}$ case, the problem is now that even though the average

correlation functions of a large set of these structures approaches zero, like for the random alloy. The variance of the average is nonzero meaning that a selected structure of the sample is prone to contain errors. The extent of these errors can be evaluated from the standard deviations

$$\nu_{k,m}(N) = | \langle \Pi_{k,m}^2 \rangle |^{\frac{1}{2}} = (D_{k,m}N)^{-\frac{1}{2}} \quad (3.10)$$

Given the computational aspects, it's obvious that economical structures with small N are prone to large errors. In fact, in some cases these errors can result in correlation functions centering around 1, as opposed to 0 for a perfect random alloy.

The degree to which a structure s fails to reproduce the property E of the ensemble-averaged property of the random alloy can be described by a hierarchy of figures

$$\langle E \rangle - E(s) = \sum_{k,m}^I D_{k,m} [(2x-1)^k - \Pi_{k,m}(s)] \epsilon_{k,m}, \quad (3.11)$$

the prime is meant to symbolize the absence of the value 0,1 for k,m . The contribution from the figure property ϵ is smaller in larger figures. In disordered systems the physical property "E" at a given point R falls off exponentially as $|R - R'|/L$, where L is a characteristic length scale relating to the specific property. Using this, the approach of SQS is to specify a set of correlation functions that hierarchically mimic the correlation functions of the random alloy. Meaning that it prioritizes the nearest neighbor interactions. With the set of functions decided on, the objective is finally to locate the structures that correspond to the selected structures.

With this approach, [9] managed by mimicking the correlation functions exact for the first two shells, to reduce the computational measures of an accurate model. In this exact study they matched the results of an $N \rightarrow \infty$ by an $N = 8$ SQS. In the next section we will take a look at recent advances made to the special quasi-random structures method and applications to high-entropy alloys.

3.1.2 Applications to high-entropy alloys

The success of the SQS method is in large part related to the fact that we can create simple periodic structures, this allows for the use of standard DFT methods to calculate with ease properties such as the total energy, charge density and electronic band structure [10], [11]. However, some certain obstacles arise when trying to apply the SQS model to high-entropy alloys. An exhaustive analysis discussing several of these factors and comparing to alternative methods were performed in 2016 by M.C Gao et al. [12] in the framework of DFT and VASP.

The first initial concern is the size of the supercell. This parameter needs to be balanced between accuracy and cost. A larger SQS cell consisting of a greater number of atoms better encapsulate the disordered structure of HEAs, but both the generation and simulation of such large SQSs come at an increased computational demand. M.C Gao discovered a

significant sensitivity between the registered stability and predicted crystal structure of CoCrFeNi and CoCrFeMnNi HEAs and varying SQSs sizes. Experimentally both of these is found stable in the FCC structure. By calculating the enthalpy of formation, he found that SQSs under 64 atoms wrongly predicted the HCP structure as the most stable, while larger SQS correctly agreed on the FCC structure. Additionally, the probability distribution functions (PDFs) of the respective SQSs display a dependence to the SQS size. For example in 3 SQSs of size 20, 125 and 250 atoms each of FCC CrFeMnNi, the Cr-Mn is much better represented in the large SQS model as seen bellow in figure 4.1.

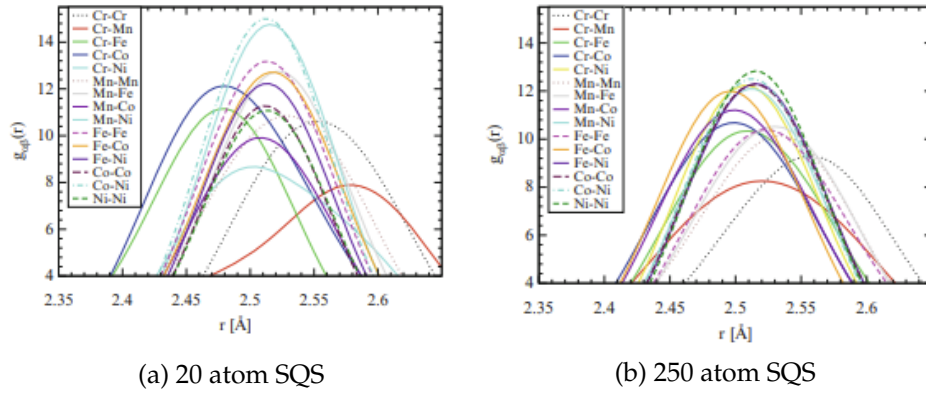


Figure 3.1: PDFs of (a) 20 and (b) 250 atom SQS models of CrFeMnNi [12]

It can also be noted that a similar dependence on the SQS size is apparent for the entropy and mechanical properties, however these topics are not relevant for this project and will thus not be elaborated further. Bellow we summarize the findings of M.C Gao et al between the SQS model and the crystal potential approximation and hybrid monte-carlo/molecular dynamics applied to high-entropy alloys. The comparison of SQS and MC/MD in terms of the calculated density of states can be seen in figure 3.2.

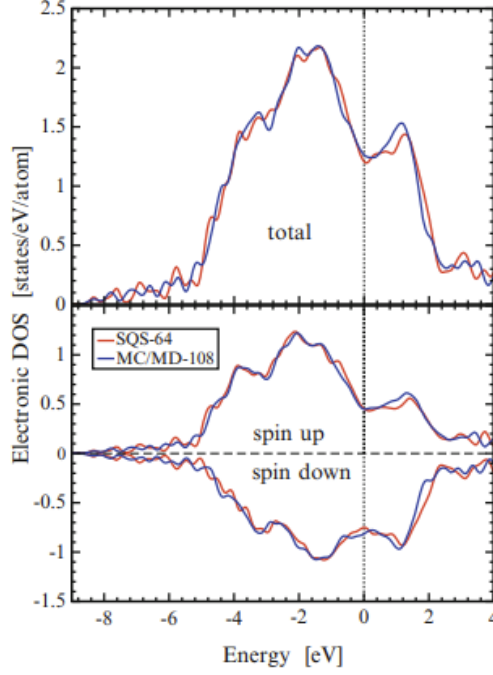


Figure 3.2: Density of states with SQS and MC/MD of FCC CoCrFeNi, figure from [12]

The density of states (DOS) of the MC/MD simulations were conducted on a larger 108 atom cell, compared to a 64 atom SQS. In despite of both the larger cell and much more complex calculations, the results of the SQS model measures up well. Furthermore, the SQS model produce a comparative outcome of the probability distribution functions (PDFs) to MC/MD as seen bellow.

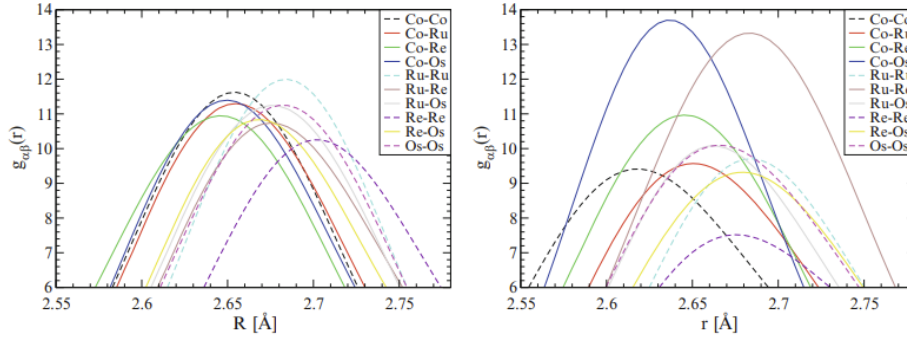


Figure 3.3: Probability distribution functions with SQS and MC/MD of HCP CoOsReRu [12]

The discrepancy in the PDFs are seen as more accurate from MC/MD calculations compared to experimental values. This is because SQS fail to include inter-atomic interaction and preference to the same extent as MC/MD. This is illustrated in figure 3.3 for the HCP CoOsreRu alloy, in which clear preference of Co-Os and Re-Ru pairs is apparent from MC/MD

simulations but not in the SQS model. Regardless, the results of SQS is very good considering the simplicity of the model and implementation. Compared to the CPA method, SQS is the less equipped method for dealing with specific cases such as $A_1/3BCDE$ structures, and paramagnetic materials [12]

We have seen up until this point that the SQS method utilized an intelligent approach which allows for a simple implementation and calculations while providing results mostly on par to other more intricate and complex solutions to model disordered structures. However one particular factor concerning SQS that does not apply for CPA and MC/MD, is that within the SQS model one material can obtain in a number of distinct configurations. For example a quaternary and quinary alloy make for 24 and 124 unique configurations respectively, resulting in an uncertainty of the energy regarding the different permutations. This effect is most prominent in anisotropic lattices such as HCP and alloys with chemically dissimilar constituents, and particularly in smaller SQSs [12].

Despite of it's flaws, especially in recent years SQS have emerged as a viable and trusted method of modeling disordered structures such as HEAs. This is down to both the increasingly available computational power and improvements to the SQS method. The latter particularly saw a boost in 2013 with the introduction of the MC-SQS method [13], short for Monte-Carlo Special Quasirandom Structures. Contrary to the original SQS method that seek to minimize the difference between the correlation functions of the approximated cell and the true random alloy, this method employ monte-carlo simulations to perfectly match a maximum number of correlation functions. Furthermore emphasizes an efficient and fast implementation in addition to an exhaustive unbiased search of possible atomic configurations. Following, this is the preferred and most widely used method of choice in today's research. This has resulted in an increased number of studies utilizing SQSs to investigate high-entropy alloys, for instance [14], [15], [16], and [17].

Chapter 4

Density Functional Theory

The density functional theory (DFT) is recognized as a overwhelmingly successful and important theory in quantum chemistry and the overall study and understanding of matter. As illustrated in figure 4.1 this is a increasingly popular method with rapid growth to this day due to improvements to both the method and computational power. The overarching goal of DFT is to efficiently solve the many-body Shrödinger equation, therefore we begin this section by reviewing central concepts of quantum mechanics such the Shrödinger equation and the various approximations one can make. Followed by an in-depth derivation of the Kohn-Sham density functional theory, and finally point out some of the limitation of DFT. The content in this section is based on the lecture notes [18] from the course FYS-MENA4111 - "Quantum Mechanical Modeling of Nanomaterials" at the University of Oslo, written by Clas Persson. In addition to the book "A practical introduction to DFT" (Sholl, Steckel) [19].

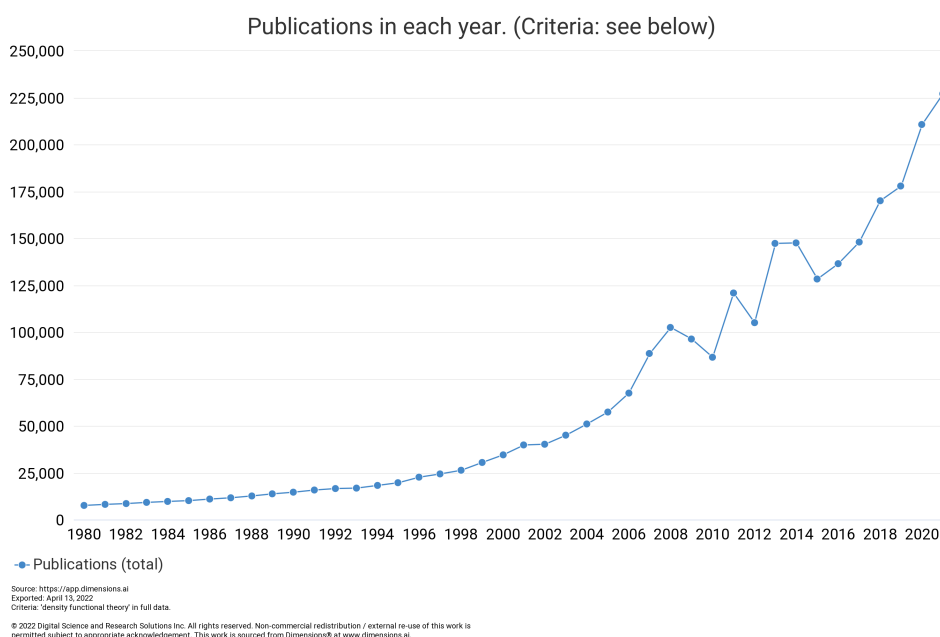


Figure 4.1: Number of DFT studies per year from 1980 to 2021 [20].

4.1 Review of Quantum Mechanics

4.1.1 The Shrödinger equation

The fundamental equation that describe materials at microscopic level is the Shrödinger equation. The time-dependent Shrödinger equation for one electron is

$$i\hbar \frac{\partial}{\partial t} \Psi(\mathbf{r}, t) = \hat{H}(\mathbf{r}, t) \Psi(\mathbf{r}, t). \quad (4.1)$$

which consists of the the wavefunction $\Psi(\mathbf{r}, t)$ to describe the electron, and the Hamiltonian $\hat{H}(\mathbf{r}, t)$ where \mathbf{r} and t is the spatial position and time. The Hamiltonian describe the total energy of the system by a kinetic part $T = \frac{-\hbar^2 \nabla^2}{2m_e}$, where m_e is the electron mass and \hbar is the Planck constant, and a potential energy operator U typically an external potential denoted $V_{ext}(\mathbf{r}, t)$.

Eigenfunctions of the Hamiltonian are denoted as $\psi_\kappa(\mathbf{r}, t)$ with an energy eigenvalue ϵ_κ for the κ eigenstate. Above we included the time-dependent Shrödinger equation, but almost all cases involving Quantum physics employ rather the time-independent Shrödinger equation in which the external potential is independent of time. This equation is given in equation 4.2 for the eigenvalues E_k of the k -th eigenfunction $\psi_k(\mathbf{r})$ as

$$\left(-\frac{\hbar^2 \nabla^2}{2m_e} + V_{ext}(\mathbf{r}) \right) \psi_\kappa(\mathbf{r}) = E_k \psi_\kappa(\mathbf{r}). \quad (4.2)$$

Solving the single electron time-independent equation often results in infinite eqienstates that the electron can occupy. The most probable state the electron occupy is the lowest energy state called the ground state, this state is indicated by $\kappa = 0$. Extending to a system comprised of multiple particles we have the many-body wavefunction Ψ^{en} in equation 4.3 and the many-body Hamiltonian H^{en} in equation 4.4. In the many-body wavefunction r_j represent the coordinates of the j :th electron and likewise R_α describe the coordinates of the α :th nucleus, and the subscript "en" indicate that both electrons and nuclei are considered

$$\Psi^{en}(\mathbf{r}, \mathbf{R}) = \Psi^{en}(r_1, r_2, \dots, r_{N_e}, R_1, R_2, \dots, R_{N_n}). \quad (4.3)$$

The many-body Hamiltonian accounts for the kinetic energy T_e of N_e electrons, the interaction energy between electrons U_{ee} , the kinetic energy of N_n nuclei, the coulomb interaction between nuclei U_{nn} , and finally the attractive interaction between nuclei and electrons U_{en} as

$$\begin{aligned}
H^{en} = & - \overbrace{\sum_{j=1}^{N_e} \frac{\hbar^2 \nabla_j^2}{2m_e}}^{T_e} - \overbrace{\sum_{\alpha=1}^{N_n} \frac{\hbar^2 \nabla_\alpha^2}{2m_n}}^{T_n} + \overbrace{\sum_{j=1}^{N_e} \sum_{j' < j} \frac{q^2}{|r_j - r_{j'}|}}^{U_{ee}} \\
& + \underbrace{\sum_{\alpha=1}^{N_n} \sum_{\alpha' < \alpha} \frac{q^2 Z_\alpha Z_{\alpha'}}{R_\alpha - R_{\alpha'}}}_{U_{nn}} - \underbrace{\sum_{j=1}^{N_e} \sum_{\alpha=1}^{N_n} \frac{q^2 Z_\alpha}{|r_j - R_\alpha|}}_{U_{en}}.
\end{aligned} \tag{4.4}$$

Combining the many-body wavefunction and the many-body Hamiltonian we get the many body Schrodinger equation with total energy eigenvalue E_κ^{en} of the whole system in eigenstate κ

$$H^{en} \Psi_\kappa^{en}(\mathbf{r}, \mathbf{R}) = E_\kappa^{en} \Psi_\kappa^{en}(\mathbf{r}, \mathbf{R}). \tag{4.5}$$

4.1.2 Approximations to the many-body Schrödinger equation

The first step in solving the many-body problem is how the many body wavefunction depends on the single electron wavefunctions. If we consider a simplified system consisting of just two electrons, the problem is reduced to finding $\Psi_\kappa(\mathbf{r}_1, \mathbf{r}_2)$ that is a function of $\psi_1(\mathbf{r}_1)$ and $\psi_2(\mathbf{r}_2)$. In the Hartree approach this is solved by assuming that the two electrons are independent of each-other and employ variable separation to express the two particle wavefunction as

$$\Psi_\kappa(\mathbf{r}_1, \mathbf{r}_2) = \psi_1(\mathbf{r}_1) \psi_2(\mathbf{r}_2). \tag{4.6}$$

The flaw of the Hartree approach is that the electrons, which are fermions, in this formulation are distinguishable and hence does not obey the Pauli exclusion principle of fermions. This is corrected by the Hartree-Fock approximation which introduces a spin function $\chi_{mp}(s_1, s_2)$ to make it anti-symmetric with respect to the particle coordinates. The Hartree-Fock approximation is expressed as

$$\Psi_\kappa(\mathbf{r}_1, \mathbf{r}_2) = \frac{1}{2} \{ \psi_1(\mathbf{r}_1) \psi_2(\mathbf{r}_2) \pm \psi_1(\mathbf{r}_2) \psi_2(\mathbf{r}_1) \} \chi_\mp(s_1, s_2). \tag{4.7}$$

The difference in energy from the improved wavefunction in Hartree-Fock compared to the Hartree approximation is called the exchange energy. Note however that Hartree-Fock is not a complete description either as it fails to model the electron correlations. For the next step we need to make use the variational principle. This is an efficient method for finding the ground state properties of a system. The method states that the energy of any trial wavefunction will always be higher than the ground-state energy E_0 , ie

$$E_0 = \langle \psi_0 | H | \psi_0 \rangle \leq \langle \psi | H | \psi \rangle = E \tag{4.8}$$

This enables us to find the ground state energy and corresponding wavefunction by a minimization technique. We will apply the variational

principle to find the ground state energy $\Psi_0(\mathbf{r}_1, \mathbf{r}_2)$ of a two electron Hartree problem. Here we skip the derivation and mechanism behind the variational principle and simply state the final product. In final, the Hartree single-electron equation is defined as

$$\left[-\frac{\hbar^2 \nabla^2}{2m_e} + V_H(\mathbf{r}) - V_{SI}(\mathbf{r}) + V_{ext}(\mathbf{r}) \right] \psi_j(\mathbf{r}) = \epsilon_j \psi_j(\mathbf{r}), j = 1, 2. \quad (4.9)$$

Furthermore the total energy can be calculated by

$$E = \sum_j \epsilon_j - \frac{1}{2} \int (V_H(\mathbf{r}) - V_{SI}(\mathbf{r})) n(\mathbf{r}) d\mathbf{r}. \quad (4.10)$$

In the above expressions V_H and V_{SI} are the Hartree potential and the self-interaction potential. The self-interaction potential is subtracted in the equations to account for that an electron can not interact with itself. The above statements can also be applied for Hartree-Fock systems and is easily extended to a N_e electron problem by setting j equal to $j = 1, 2, \dots N_e$. In this case it's common to also include the self-interaction term to simplify the calculations by making the total potential in equation. (5.10) equal for all electrons, however this introduces a self-interaction error in the approximation. Moreover, by employing the variational principle, the many body equation has been transformed to a set of single electron equations, however the use of the variational principle means that this expression is valid only for the ground state.

A second essential approximation to the many-body equation is the Born-Oppenheimer approximation. Given that the electron mass is negligibly small in comparison to that of a nuclei, we can treat the nuclei as point charges, enabling us to divide the eigenfunction into a separate electronic and nuclear part

$$\Psi_k^{en}(\mathbf{r}, \mathbf{R}) \approx \Psi_k(\mathbf{r}, \mathbf{R}) \cdot \Theta_k(\mathbf{R}), \quad (4.11)$$

In equation 4.11 $\Psi_k(\mathbf{r}, \mathbf{R})$ is the electronic part and $\Theta_k(\mathbf{R})$ the nuclear part. The \mathbf{R} dependence in $\Psi_k(\mathbf{r}, \mathbf{R})$ originate from the fact that electrons can respond instantaneously to updated positions of the nuclei. Writing this in terms of the Hamiltonian give

$$(T_e + U_{ee} + U_{en}) \Psi_k(\mathbf{r}, \mathbf{R}) = E_k(\mathbf{R}) \Psi_k(\mathbf{r}, \mathbf{R}) \quad (4.12)$$

$$(T_n + U_{nn} + E_k(\mathbf{R})) \Theta_k(\mathbf{R}) = E_k^{en}(\mathbf{R}) \Theta_k(\mathbf{R}). \quad (4.13)$$

We observe that the two sections are interrelated through the electronic energy $E_k(\mathbf{R})$. Furthermore, the left hand side of the nuclear part can be simplified to $U_{nn} + E_k(\mathbf{R})$, assuming that the kinetic energy of point charges is zero.

4.2 Kohn-Sham density functional theory

With the Hartree, Hartree-Fock and Born-Oppenheimer approximations we are finally ready to tackle the many-body Schrödinger equation. However despite the aforementioned approximations one can apply, the many-body equation still pose a few obstacles to overcome both numerically and theoretically. The first of which is how the immense number of terms in equation 4.5 can be handled in a numerical manner. As an example, a material of volume equal to 1cm^3 contain about 10^{23} nucleus and electrons which makes for nearly 10^{40} terms to solve. A second and more present concern is how the many-particle wavefunction Ψ^{en} is related to the single-particle wavefunctions, and how can we operate the Hamiltonian on Ψ^{en} . This is where the density-functional theory enters. When people mention DFT today, most of the time they mean Kohn-Sham density functional theory, that combines the concept of the original density functional theory with the Kohn-Sham equation.

4.2.1 Density functional theory

The density functional theory was developed by Hohenberg and Kohn in 1964 and centers around the ground-state density of a system

$$n_0(\mathbf{r}) = |\Psi_0(\mathbf{r})|^2. \quad (4.14)$$

The working principles of DFT is outlined in two theorems known as the Hohenberg-kohn theorems:

1. "All ground-state properties of the many-body system are determined by the ground state density $n_0(\mathbf{r})$. Each property is thus a functional $f[n]$ and the ground-state property is obtained from $f[n_0]$ ".
2. "There exists a variational principle for the energy density functional such that, if n is not the electron density of the ground-state, then $E[n_0] < E[n]$ ".

The first theorem state that the ground-state properties of a system can be determined uniquely from the ground-state density, thus the computational complexity of solving the many-body equation with $3N_e$ variables is reduced to a problem comprised of just 3 variables (x, y, z) from the density. While the second theorem provides a method of finding the ground-state density. The total energy of the system can thus be expressed as a functional of the density

$$E[n] = F[n] + \int V_{en}(\mathbf{r})n(\mathbf{r})d\mathbf{r}, \quad (4.15)$$

where $F[n] = T[n] + U_{ee}[n]$ make up the Hohenberg-Kohn functional and $\int V_{en}(\mathbf{r})n(\mathbf{r})d\mathbf{r} = U_{en}[n]$. Note that $F[n]$ is independent of the external potential, hence is universal for all systems.

4.2.2 The Kohn-Sham Equation

The working principle of Kohn-Sham density functional theory is to utilize the Kohn-Sham equation to determine the ground-state density, and then invokes the theorems of DFT to find the ground state energy. The Kohn-Sham approach begins by approximating the many-particle wavefunction by Hartree type functions

$$\Psi(\mathbf{r}_1, \mathbf{r}_2, \dots, \mathbf{r}_{N_e}) = \psi_1^{KS}(\mathbf{r}_1) \psi_2^{KS}(\mathbf{r}_2) \dots \psi_{N_e}^{KS}(\mathbf{r}_{N_e}), \quad (4.16)$$

where ψ_j^{KS} are auxiliary independent single-particle wavefunctions. This means that the density can be calculated as

$$n(\mathbf{r}) = \sum_{j=1}^{N_e} |\psi_j^{KS}(\mathbf{r})|^2. \quad (4.17)$$

The idea behind the Kohn-Sham equation is to now rewrite the energy expressed in equation 4.15 as

$$E[n] = T_s[n] + U_s[n] + U_{en}[n] + \left\{ (T[n] - T_s[n]) + (U_{ee}[n] - U_s[n]) \right\}, \quad (4.18)$$

with the "s" subscript relating to that the wavefunctions are the auxiliary wavefunctions as described above. The enclosed term in equation (4.18) is known as the exchange-correlation energy E_{xc} of the system, defined as $E_{xc}[n] = \Delta T + \Delta U$. This quantity contains the leftover energy between the exact energy and the energy corresponding to the simpler terms $T_s[n] + U_s[n] + U_{en}[n]$. This means that the exchange-correlation must account for the more complex energies corresponding to the many-electron interaction, electron self-interaction and the kinetic energy part. Thus if E_{xc} is exact, so is the total energy. In full, we can write the energy functional as

$$\begin{aligned} E[n] = & \overbrace{\sum_j \int \psi_j^{KS*} \frac{-\hbar^2 \nabla^2}{2m} \psi_j^{KS} d\mathbf{r}}^{T_s[n]} + \overbrace{\frac{1}{2} \int \int q^2 \frac{n(\mathbf{r})n(\mathbf{r}')}{|\mathbf{r} - \mathbf{r}'|} d\mathbf{r}d\mathbf{r}'}^{U_s[n]} \\ & + \underbrace{\int V_{en}(\mathbf{r})n(\mathbf{r})d\mathbf{r}}_{U_{en}[n]} + \underbrace{(T[n] - T_s[n]) + (U_{ee}[n] - U_s[n])}_{E_{xc}[n]} \end{aligned} \quad (4.19)$$

Analog to how we derived the single-particle Hartree equation, the single-particle Kohn-Sham equation can be derived with the variational principle to yield

$$\left\{ -\frac{\hbar^2}{2m_e} \nabla_s^2 + v_H(\mathbf{r}) + V_{en}(\mathbf{r}) + V_{xc}(\mathbf{r}) \right\} \psi_s^{KS}(\mathbf{r}) = \epsilon_s^{KS}(\mathbf{r}) \psi_s^{KS}(\mathbf{r}). \quad (4.20)$$

The ground-state density in equation 4.17 can now be calculated by solving the single-particle Kohn-Sham equation for all ground state single electron wavefunctions. Finally, we arrive at the total ground-state energy of the system

$$E[n] = \sum_j \epsilon_j^{KS} - \frac{1}{2} \int V_H(\mathbf{r}) n(\mathbf{r}) d\mathbf{r} + E_{xc}[n] - \int V_{xc}(\mathbf{r}) n(\mathbf{r}) d\mathbf{r}, \quad (4.21)$$

where $V_{xc}(\mathbf{r}) = \frac{\partial E_{xc}[n]}{\partial n}$ is the exchange-correlation potential. This is the Kohn-Sham density functional theory.

4.3 Limitations of DFT

The primary drawback of the density functional theory is that to this day we still don't have the exact form of E_{xc} . From the above derivations we recognize that this term must account for several complex properties such as the many-body interaction and large amounts of kinetic energy. Additionally the exchange-correlation must also include the self-interaction error from applying Hartree-like wavefunctions in the Kohn-Sham equation. Furthermore this functional should be applicable in any material, ie metals, semiconductors, liquids and gasses. In the next section we will look at some of the most commonly used approximations to E_{xc} . These approximate functionals range from low-complex and computationally cheap methods such as LDA, to heavy computational methods such as hybrid functionals. This is therefore seen as a disagreement between the theoretical philosophy of the DFT and the practical application of it, ie in practice one must adapt the functional first to the type of system and intention, for example if one wants to study the band gap, or weak Wan-Der Waals interactions. Secondly the functional must be chosen as a compromise between accuracy and cost.

However, even if the exchange-correlation functional was expressed exactly and efficiently implemented, DFT would still serve a couple of drawbacks. For instance the Kohn-Sham eigenfunctions in equations 17 are not the true single-electron eigenfunctions, thus also the corresponding eigenvalues are not exact even with an exact value of E_{xc} , meaning that the band gap obtained from the eigenvalues is in nature inexact. In fact, the estimation of the band gap of semiconductors is one of the major shortcomings of DFT. In addition to the eigenvalue, the band gap is also subject to underestimation due to a self-interaction term that over-delocalize the occupied states and hence pushes them up in energy, effectively reducing the band gap [21]. More advanced topics regarding the under-estimation of the band gap in semiconductors from DFT calculations can be read about in [22], by John P. Perdew and Mel Levy. Additionally, DFT also have difficulties in simulating weak long-range Wan-der Waal attraction [23], due to DFT's emphasis on primarily the local density.

More practical limitations of DFT include factors such as the calculations not being variational with respect to the functional, meaning

that a more complex functional does not guarantee higher accuracy [24]. Moreover the calculations of DFT only deliver a local minimum, in other words the calculations only return the most stable energy for the given initial settings and parameters. An example of this is studying magnetic materials, where the total energy of a DFT calculation vary between each magnetic configuration of the material, meaning that to obtain the true ground-state energy one must perform an exhaustive search of all magnetic possibilities. Similar is also the case when comparing crystal structures and geometric features of materials. Finally, despite the possibility of simulations of excited states exists today, DFT in its original formulation is only valid for the ground state. Thus these calculations have a lesser theoretical footing in comparison.

Regardless of its' flaws, DFT is still considered a widely successful method and accordingly Walter Kohn and John A. Pople won the Nobel prize in chemistry in 1998; "to Walter Kohn for his development of the density-functional theory and to John Pople for his development of computational methods in quantum chemistry." [25]

Part II

Method

Chapter 5

Practical aspects of DFT

5.1 The Exchange-Correlation functional

From the former section, we know that the one piece of information missing of the density functional theory is the complex exchange-correlation energy $E_{xc}[n]$ that must account for all the simplifications and approximations employed in Kohn-Sham DFT. In this section we will explore some of the commonly used approximations to exchange-correlation functional. In this project we limit ourselves to 4 levels of complexity, first is the local density approximation (LDA), followed by the generalized gradient approximation (GGA). These two are the least complex and computationally affordable methods. Next is the methods such as meta-GGA implementations and finally the very accurate, but equally demanding hybrid-functionals. In addition, we have methods such as DFT+U, the Minnesota functionals, and double hybrids plus more, but these are outside the scope of this project.

5.1.1 Local density approximation

A homogeneous electron gas (HEG) is the sole case we know of where the exchange-correlation functional can be determined exactly, because in this simple case the electron density is constant. The LDA works by setting the exchange-correlation potential $V_{xc}(\mathbf{r})$ at every position equal to that of the homogeneous electron gas, ie

$$V_{xc}(\mathbf{r}) = V_{xc}^{\text{HEG}}[n(\mathbf{r})]. \quad (5.1)$$

Obviously the LDA is of limited use given that a large part of what makes materials interesting is the variation in the electronic density. In the case of limitations LDA is for example known to overestimate binding energies and underestimate the band gap in semiconductors and insulators. On the other hand, LDA provide generally adequate results in bulk materials with slowly varying charge density, for example equilibrium distances and vibrational frequencies. The biggest upside of LDA however comes from the low computational cost, and was one of the first big success-stories of DFT.

5.1.2 Generalized gradient approximation

A natural succession to the local density approximation is the family of generalized gradient approximation (GGA) that also include the gradient of the electron density

$$V_{\text{XC}}^{\text{GGA}}(\mathbf{r}) = V_{\text{XC}}[n(\mathbf{r}), \nabla n(\mathbf{r})]. \quad (5.2)$$

The way one can implement the gradient are plenty-full and complicated. Two of the most common methods are the Perdew-Wang 91 (PW91) [26] and the Perdew-Burke-Ernzerhof (PBE) GGA [27]. This project will utilize the latter, which came to fruition in 1996 in an article by Perdew, Burke and Ernzerhof appropriately named "Generalized Gradient Approximation Made Simple". The key point regarding the PBE functional is that it's a non-empirical method thus providing reliable and adequate accuracy over a wide range of systems, as compared to for instance the BLYP functional that provide excellent accuracy of organic molecules but fails in other cases [28].

5.1.3 Meta-GGA

Meta-GGA functionals is the final level of complexity of the non-empirical approximations to the exchange-correlation functional. In addition to the the constant density (LDA) and local gradient of the density (GGA), meta-GGA methods consider the kinetic energy density of the occupied Kohn-Sham orbitals [29]

$$\tau_{\omega} = \sum_i^{\text{occ}} \frac{1}{2} |\nabla \psi_{i\omega}|^2. \quad (5.3)$$

The role of this quantity on the the calculated band gap is well described in [30]. In this project we employ a meta-GGA functional named *Strongly Constrained Appropriately Normed*, or SCAN. This functional is the only known functional to satisfy all 17 known exact constraints of the XC functional [31]. The SCAN functional have found evidence of particularly superior accuracy of energies and geometries especially in diversly bonded structures [32], and some indication of improved band gaps and density of states over GGA and LDA functionals [33]. However delivers overall less accurate band gaps compared to other meta-GGA functionals such as the *modified Becke-Johnson* [34]. Unfortunately, MBJ proved too difficult to converge for the particular materials in this project and we instead opt for SCAN.

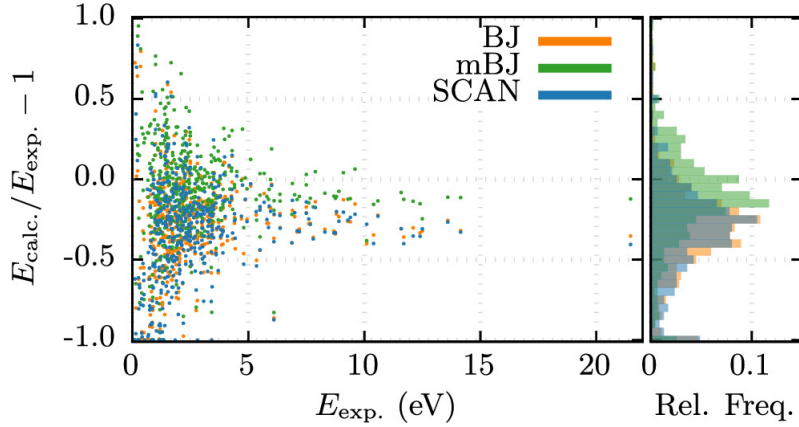


Figure 5.1: Calculated to experimental band gap measurements of Becke-Johnson, modified Becke-Johnson and SCAN functionals [35]

5.1.4 Hybrid functionals

The most accurate functional we employ in this project belong to the family of *hybrid functionals*. Accordingly this method consist of a hybrids between simpler functionals such as LDA, PBE or even meta-GGA and the exact treatment of exchange energy from Hartree-Fock, for example the global hybrid functional PBE0 [36] described as

$$E_{xc}^{PBE0} = (1 - \alpha)E_x^{PBE} + \alpha E_x^{HF} + E_c^{PBE}, \quad (5.4)$$

where α is the mixing parameter to decide the balance between the exchange energy, denoted x of Hartree-Fock with PBE. Alike the last term represent the correlation energy from the PBE functional. This parameter alpha is determined empirically, thus making hybrid functional a semi-empirical model. Obviously considering the exact exchange in Hartree-Fock is a computationally challenging prospect. Heyd-Scuseria-Ernzerhof managed to lower the cost by the concept of Screened functionals that separate the Coloumb interaction into long-range and short-range interaction by a function $erfc(\mu r)$. These are known as HSE functionals [37], one of the superior methods for accurate band gaps is the HSE06 hybrid functional [38], with $\alpha = 0.25$ and $\mu = 0.11$.

5.1.5 Outlook

In many cases LDA and GGA suffice, PBE especially is by most considered the conventional standard for DFT calculations, for its balance of accuracy, cost and wide range applicability. However, distinctly concerning the band gap of a solids, both of these fall short. This is because the band gap of DFT calculations is complicated by the fact that the derivative of the XC-functional is discontinues with respect to the electron concentration [39], thus the simpler functionals fail to recall the experimental values since the total band gap in DFT is the fundamental gap (valence - conduction) + this contribution. This is corrected in meta-GGA and hybrid functionals

in the generalized Kohn-Sham scheme. Lastly, we would like to refer the reader to the work of Borlido, Aull, Huran, Tran, Marques, and Botti whom in 2019 conducted an exhaustive investigation of the band gap of over 470 unique non-magnetic compounds in order to benchmark the relative performance of several of the available and widely used XC-functionals [35]. In this large-scale project they found overwhelming confirmation that the HSE06 functional followed closely by Modified-Becke Johnson is the superior choice for accurate band-gap measures. Regarding the SCAN functional, in several cases this yielded outputs very comparable to MBJ, and produce much better formation energies than PBE, but tends to overestimate in magnetic alloys. On the other side both LDA and PBE resulted in 50% and 30% under-estimation of the band gap or in several cases miss-classified compounds as metals, this was particularly evident in materials containing Ni and other 3d elements.

5.2 Plane waves and reciprocal space

The solution of the Schrödinger equation for a free electron have a simple analytic solution $\psi_k = Ae^{ikr}$. In a crystalline matter with a periodic potential $V(\mathbf{r}) = V(\mathbf{r} + \mathbf{R})$, the single-electron wavefunction takes the form

$$\psi_k(\mathbf{r}) = u_k(\mathbf{r})e^{i\mathbf{k}\cdot\mathbf{r}}, \quad (5.5)$$

where $u_k(\mathbf{r})$ is a Bloch wave with the periodicity of the crystal and $e^{i\mathbf{k}\cdot\mathbf{r}}$ is called a plane wave. Because we use plane waves, DFT calculations are often referred to as plane wave calculations. The Bloch wave is the sum of all plane waves with wave vector equal to the reciprocal wave vector \mathbf{G} , described as

$$u_k(\mathbf{r}) = \sum_{\mathbf{G}} c_{\mathbf{G}} e^{i\mathbf{G}\cdot\mathbf{r}}, \quad (5.6)$$

which gives us the final expression for $\psi_k(\mathbf{r})$

$$\psi_k(\mathbf{r}) = \sum_{\mathbf{G}} c_{\mathbf{k}+\mathbf{G}} e^{i(\mathbf{k}+\mathbf{G})\cdot\mathbf{r}} \quad (5.7)$$

Clearly, the infinite summation over all \mathbf{G} necessary to evaluate the wavefunction at a single point in reciprocal space is computationally unfeasible. In order to reduce this computational burden, we can introduce a maximum cutoff value of the energy E_{cut} . This is possible because equation 5.7 is the solution of the Schrödinger equation with corresponding kinetic energy

$$E = \frac{\hbar^2}{2m} |\mathbf{k} + \mathbf{G}|^2. \quad (5.8)$$

Assuming that the lower energy solutions are the most interesting, we can limit the calculations to plane waves with energy less than E_{cut} as

$$E_{\text{cut}} = \frac{\hbar^2}{2m} G_{\text{cut}}^2. \quad (5.9)$$

Thus, we can reduce the infinitely large sum above to a much more feasible calculation

$$\psi_{\mathbf{k}}(\mathbf{r}) = \sum_{|\mathbf{k}+\mathbf{G}| < G_{\text{cut}}} u_{\mathbf{k}+\mathbf{G}}(\mathbf{r}) e^{i(\mathbf{k}+\mathbf{G})\mathbf{r}}. \quad (5.10)$$

The cutoff energy is determined by performing a number of calculations of different cutoff and observe the convergence with respect to the total energy of the system. Another important parameter to specify in DFT calculations is the number of k-points. As seen in the above expression the wavevector \mathbf{k} plays a big role in DFT, an other case that is more convinient to calculate in k-space is integrals of the from

$$g = \frac{V_{\text{cell}}}{(2\pi)^3} \int_{\text{BZ}} g(\mathbf{k}) d\mathbf{k}, \quad (5.11)$$

for instance the density of states. Note that "BZ" indicate that the integral is evaluated for all \mathbf{k} in the Brillouin zone. This integral can be approximated by evaluating it at a set of discrete k-points in reciprocal space and summing over the points with appropriately assigned weights. A larger set of points leads to more exact approximations. The method for selecting k-points in reciprocal space was developed by Monkhorst and Pack in 1976, where one specify a number of points in each dimension $N_x N_y N_z$. Recalling that reciprocal space is inverse to regular space, supercells with equal and large dimensions converge at smaller values of N, and inversly for cells of small dimsion. The total number of k-points required for accurate can be reduced by utulizing the symmetry of the cell, in which we can exactly approximate the entire BZ by extending a lesser zone through symmetry of the crystal lattice. This reduced zone is named the irreducible Brillouin zone (IBZ).

The required number of k-points for a given calculation can be found alike the cutoff energy by performing convergence tests with respect to the total energy of the system. Metals in particular require a large number of k-points because of discontinues integrals in the Brillouin zone around the Fermi surface where the states discontinuously change from occupied to non-occupied. To reduce the cost of this operation, there are two primary methods, tetrahedon and smearing. The idea behind the tetrahedon method is to use the discrete set of k-points to fill the reciprocal space with tethraeda and interpolate the function within each tethraeda such that the function can be integrated in the entire space rather than at discrete points. The latter approach for solving discontinuos integrals is to smear out the discontinuity and thus transforming the integral to a continuous one. A good analogy to this method is the fermi-dirac function, in which a small variable σ transform a step-function into a continuous function that can be integrated by standard methods.

A final consideration to how DFT is applied in practice is how the core electrons are handled. Tightly bound core electrons as opposed to valence electrons demand a greater number of plane-waves to converge. The most efficient method of reducing the expenses of core-electrons are

so-called pseudopotentials. This method works by approximating the electron density of the core electrons by a constant density that mimic the properties of true ion core and core electrons. This density is then remained constant for all subsequent calculations, in other words only considering the valence electrons while regarding the core electrons as frozen-in. There are currently two popular types of pseudopotentials used in DFT, so-called ultrasoft pseudopotentials (USPPs) developed by Vanderbilt, and the projector augmented-wave (PAW) method by Bloch [40], [41].

5.3 Self-consistent field calculation

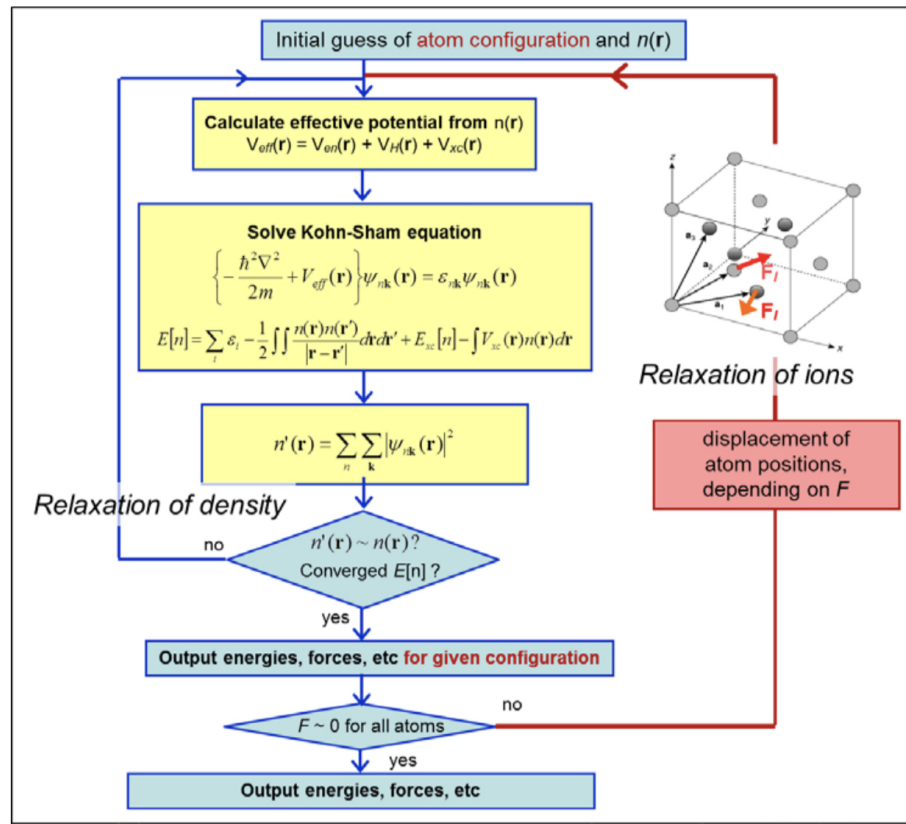


Figure 5.2: Self consistent iteration of a DFT calculation. Figure adopted from lecture notes fys-mena4111 [18]

Preluding this section, we have considered the fundamental theory of DFT and it's practical ability to model various materials. Figure 5.2 illustrate the self-consistent field calculation scheme for how DFT calculations are performed in practice. The initial problem posed by DFT is that all properties rely on the density, and are following dependent on each other. For instance, the effective potential is dependent on the density, which again is dependent on the eigenfunctions, that rely on the effective potential again. The cleaver approach begin with an initial guess to the density from which we can solve the Kohn-Sham equation and obtain the

corresponding eigenfunctions. Following is an iterative method where we apply the recently calculated eigenfunctions to determine a new density and repeat the procedure above. This is repeated until the total energy is converged, by an own-defined criterion. Equivalently, the optimal ionic positions can be found by a similar approach. This method is based on quasi-Newton algorithms to minimize the forces between ions.

Chapter 6

Computational details

Materials project citation: [42]

6.1 Vienna Ab initio Simulation Package

This software, often referred to as VASP is a package for ab initio quantum mechanics calculations using the projected augmented wave method and plane wave basis set. The intended methodology is DFT, but have been extended for methods post the original DFT-formulation. Calculations with VASP was carried out on the supercomputer fram, with allocated time and resources provided by Uninett Sigma2,**add reference!**

The structure of VASP rely on a set of input files and output files from the calculation, the input files required to perform a DFT computation in VASP are the following:

- INCAR - this file provide the tags responsible for different methods, algorithms, parameters etc.
- POSCAR - this file is related to the crystal structure of the system
- POTCAR - What psudopotential that is used
- KPOINTS - A file containing information on what KPOINTS will be used
- jobfile - This file contains information for the supercomputer regarding resources and such.

The capitalization displayed above is directly related to the requirements of the file system in the VASP/fram collaboration. Some important output files are:

- CONTCAR - The relaxed crystal structure after finalized calculation
- CHGCAR - This file contains the electron density after calculation
- EIGENVAL - Contains the solutions to the Kohn-Sham eigenfunctions

- DOSCAR - Information on the Density of States
- OUTCAR - Contains a list of all other information.

Some figure or tables to make this information more presentable

In this project, we used the PAW pseudopotential, and PBE GGA in favor of LDA for the reasons mentioned previously. Furthermore we readily employed meta-GGA functionals and hybrid-functionals, in particular SCAN and HSE06. We began the calculation of every individual structure by testing the convergence of total energy with respect to the number of k-points and cutoff energy. In VASP, the latter can be specified by setting the tag "ENCUT" in the INCAR file, we found 300 eV to yield productive results in terms of convergence and computation time for total energy calculations, and 400 for ionic+volume relaxations. Regarding the number of points in the reciprocal space, we carried out a great deal of simulations on numerous structures with distinct crystal structures and corresponding supercells, for this reason we employed a number of different sets of k-points depending on the structure. Typically the number of points ranged from a 2x2x2 mesh to 4x4x4 mesh. With the smaller being required for hybrid functionals to converge.

Upon realizing the convergence parameters, the structures were allowed to relax both the ionic positions, and cell volume with the quasi-newton method and a convergence criterion of $1E - 2$ for the forces and $1E - 5$ for the total energy. However, the symmetry of the structure was forced constant by the use of vasp-std-noshear. This process was repeated two times before performing final total energy calculation with various functionals.

The specific tags, algorithms, parameters and options of VASP that was in use throughout this project can be found at our GitHub address, but in particular we would like to cover two specific parameters. The First is related to the magnetic configuration of our calculations, specified with the tag ISPIN in VASP. We used ISPIN=2 which allow for co-linear spin-polarized calculations due to the involvement of ferromagnetic elements such as iron and nickel in this study. However, there are many more magnetic orientations the system can adopt besides co-linear, therefore the final total energies we found may not be the true lowest energies. But given the allocated duration and resources of this project, this is a understood consequence. Secondly is the type of smearing that was used for the different calculations. The preferred method for accurate total energies and density of states in semiconductors is the tetrahedron method [43], and for accurate forces in metals the Methfessel-Paxton method is recommended. However, our system contains both metals and a large portion of Si. For this reason we used a combination of smearing methods. For the relaxation and minimization of forces, we used gaussian smearing with smearing width $\sigma = 0.05$, as this method provide accurate forces in both metallic and semiconducting materials. And to calculate the total energy and DOS, we used the tetrahedron method, as recommended. In order to obtain converged results of the HSE06 functional, we first calculated the charge density with gaussian smearing, then apply this density to perform

a second hybrid calculation with the tetrahedron method. This was necessary because gaussian smearing yielded inaccurate and unreliable results in terms of the density of states when comparing to the band gap from the koh-Sham eigenvalues. However, this method, in addition to the narrow k-grid of just 2x2x2 k-points does include a factor of uncertainty regarding these results from the HSE06 functional.

This [44] is a good reference for extracting the band gap of VASP jobs relating to smearing and DOSCAR vs EIGENVAL

Band structure/DOS and band-unfolding?

6.2 Material

Needs work, add part on filling ratio of ideal cube The generation of special quasi-random structures as described in section .., was done by utilizing the Temperature Dependent Effective Potential (TDEP) method. This package, devolved by Olle Hellman, offers a wide range of tools primary intended for studies of finite temperature lattice dynamics. In this project we utilize the program generate-structure within the TDEP package to construct SQS's. The work of TDEP is the result of an unpublished PHD thesis by Nina Shulumba (**Insert citation**), thus the documentation on the software and generate-structure script is limited, please refer to the original author for more information.

In this project, we constructed SQS's by first transforming the cif-files of a given initial structure, for instance that of $FeSi_2$, to a primitive unit cell. The SQS's was generated by the same principles explained in section .., for each structure we created 5 distinct SQS's of an equal size under the constraint that the 3d atoms be distributed eqvimolar in the system. Precise file formats and such can be found at GitHub. Another approach could have been to construct SQS's of specific cell counts instead of total number of atoms, however this quickly lead to extremely large supercells, up to 256 atoms, that simply would not converge to our best efforts.

We began by studying high-entropy silicides by alloying 3d-metal silicides such as Fe_2Si by Cr, Fe, Co, and Ni to construct a $(CoCrFeNi)_2Si$ alloys. From this point we varied the distribution and type of elements in an attempt to locate high-entropy silicides with semiconducting properties, but remained within quaternary 3d silicides. Examples of SQSs generated by TDEP, from $FeSi_2$ structure with Cr, Fe, Mn and Ni can be seen in figure 6.1.

The $FeSi_2$ structure consisted of 48 atoms, 16 of which is iron and the remaining 32 sites occupied by silicon atoms. We filled the 16 iron sites with an even distribution of chromium, iron, manganese and nickel by the principle of the SQS method described in section .. . With this approach, there are many possible supercells one can create, we however limit ourself to 5 distinct supercells per composition, which means that we have 5 structures of the same composition and space group, but the distribution is slightly different. This allow us to both study a composition to great depth, but also to test different compositions and structures, compared to if we in-

stead generated 10 or 15 or more supercells. But its important to be aware of this assumption, as our results may be subject to errors and result that does not match the true random alloy due to a small sample size.

In the figure bellow this and that color represent this and that element.

6.3 Work flow and dependencies

During the course of the projects lifetime, several shell and python scripts was developed by myself and/or provided to me by my supervisor Ole Martin Løvvik and his team of researchers at Sintef. These can be located at the GitHub address :...

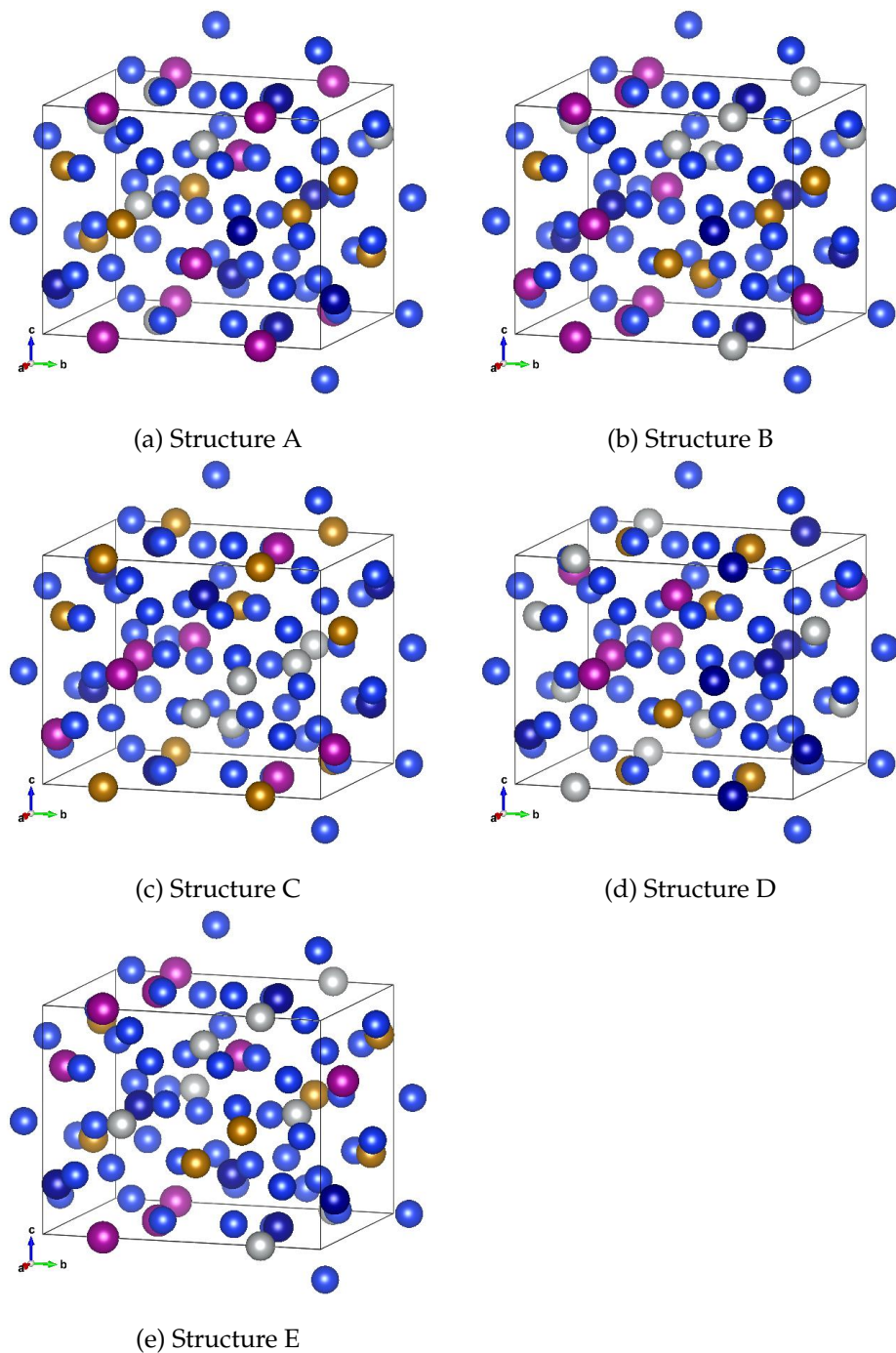


Figure 6.1: 48 atom SQS based on eqvimolar distribution of Cr, Fe, Mn and Ni in and $FeSi_2$ cell.

Part III

Results and Discussion

Part IV

Conclusion

Write conclusion here

Bibliography

- [1] Jien-Wei Yeh. 'Overview of High-Entropy Alloys'. In: *High-Entropy Alloys: Fundamentals and Applications*. Ed. by Michael C. Gao et al. Cham: Springer International Publishing, 2016, pp. 1–19. ISBN: 978-3-319-27013-5. DOI: 10.1007/978-3-319-27013-5_1. URL: https://doi.org/10.1007/978-3-319-27013-5_1.
- [2] Yong Zhang et al. 'Phase Formation Rules'. In: *High-Entropy Alloys: Fundamentals and Applications*. Ed. by Michael C. Gao et al. Cham: Springer International Publishing, 2016, pp. 21–49. ISBN: 978-3-319-27013-5. DOI: 10.1007/978-3-319-27013-5_2. URL: https://doi.org/10.1007/978-3-319-27013-5_2.
- [3] Jien-Wei Yeh. 'Physical Metallurgy'. In: *High-Entropy Alloys: Fundamentals and Applications*. Ed. by Michael C. Gao et al. Cham: Springer International Publishing, 2016, pp. 51–113. ISBN: 978-3-319-27013-5. DOI: 10.1007/978-3-319-27013-5_3. URL: https://doi.org/10.1007/978-3-319-27013-5_3.
- [4] Jien-Wei Yeh et al. 'Functional Properties'. In: *High-Entropy Alloys: Fundamentals and Applications*. Ed. by Michael C. Gao et al. Cham: Springer International Publishing, 2016, pp. 237–265. ISBN: 978-3-319-27013-5. DOI: 10.1007/978-3-319-27013-5_7. URL: https://doi.org/10.1007/978-3-319-27013-5_7.
- [5] Lewis Robert Owen and Nicholas Gwilym Jones. 'Lattice distortions in high-entropy alloys'. In: *Journal of Materials Research* 33.19 (2018), pp. 2954–2969. DOI: 10.1557/jmr.2018.322.
- [6] Tingting Zuo et al. 'Tailoring magnetic behavior of CoFeMnNiX (X = Al, Cr, Ga, and Sn) high entropy alloys by metal doping'. In: *Acta Materialia* 130 (2017), pp. 10–18. ISSN: 1359-6454. DOI: <https://doi.org/10.1016/j.actamat.2017.03.013>. URL: <https://www.sciencedirect.com/science/article/pii/S1359645417302008>.
- [7] Oldřich Schneeweiss et al. 'Magnetic properties of the CrMnFeCoNi high-entropy alloy'. In: *Phys. Rev. B* 96 (1 July 2017), p. 014437. DOI: 10.1103/PhysRevB.96.014437. URL: <https://link.aps.org/doi/10.1103/PhysRevB.96.014437>.
- [8] Fuyang Tian. 'A Review of Solid-Solution Models of High-Entropy Alloys Based on Ab Initio Calculations'. In: *Frontiers in Materials* 4 (2017). ISSN: 2296-8016. DOI: 10.3389/fmats.2017.00036. URL: <https://www.frontiersin.org/article/10.3389/fmats.2017.00036>.

- [9] S.-H. Wei et al. 'Electronic properties of random alloys: Special quasirandom structures'. In: *Phys. Rev. B* 42 (15 Nov. 1990), pp. 9622–9649. DOI: 10.1103/PhysRevB.42.9622. URL: <https://link.aps.org/doi/10.1103/PhysRevB.42.9622>.
- [10] Z. W. Lu, S.-H. Wei and Alex Zunger. 'Electronic structure of ordered and disordered Cu_3Au and Cu_3Pd '. In: *Phys. Rev. B* 45 (18 May 1992), pp. 10314–10330. DOI: 10.1103/PhysRevB.45.10314. URL: <https://link.aps.org/doi/10.1103/PhysRevB.45.10314>.
- [11] Su-Huai Wei and Alex Zunger. 'Band offsets and optical bowings of chalcopyrites and Zn-based II-VI alloys'. In: *Journal of Applied Physics* 78.6 (1995), pp. 3846–3856. DOI: 10.1063/1.359901. eprint: <https://doi.org/10.1063/1.359901>. URL: <https://doi.org/10.1063/1.359901>.
- [12] Michael C. Gao et al. 'Applications of Special Quasi-random Structures to High-Entropy Alloys'. In: *High-Entropy Alloys: Fundamentals and Applications*. Ed. by Michael C. Gao et al. Cham: Springer International Publishing, 2016, pp. 333–368. ISBN: 978-3-319-27013-5. DOI: 10.1007/978-3-319-27013-5_10. URL: https://doi.org/10.1007/978-3-319-27013-5_10.
- [13] A. van de Walle et al. 'Efficient stochastic generation of special quasirandom structures'. In: *Calphad* 42 (2013), pp. 13–18. ISSN: 0364-5916. DOI: <https://doi.org/10.1016/j.calphad.2013.06.006>. URL: <https://www.sciencedirect.com/science/article/pii/S0364591613000540>.
- [14] Shen Wang et al. 'Comparison of two calculation models for high entropy alloys: Virtual crystal approximation and special quasi-random structure'. In: *Materials Letters* 282 (2021), p. 128754. ISSN: 0167-577X. DOI: <https://doi.org/10.1016/j.matlet.2020.128754>. URL: <https://www.sciencedirect.com/science/article/pii/S0167577X20314610>.
- [15] Peng Wei et al. 'Understanding magnetic behaviors of $\text{FeCoNiSi}_{0.2}\text{M}_{0.2}$ ($\text{M}=\text{Cr}, \text{Mn}$) high entropy alloys via first-principle calculation'. In: *Journal of Magnetism and Magnetic Materials* 519 (2021), p. 167432. ISSN: 0304-8853. DOI: <https://doi.org/10.1016/j.jmmm.2020.167432>. URL: <https://www.sciencedirect.com/science/article/pii/S0304885320323994>.
- [16] Muhammad Rashid et al. 'Ab-initio study of fundamental properties of ternary $\text{ZnO}_{1-x}\text{S}_x$ alloys by using special quasi-random structures'. In: *Computational Materials Science* 91 (2014), pp. 285–291. ISSN: 0927-0256. DOI: <https://doi.org/10.1016/j.commatsci.2014.04.032>. URL: <https://www.sciencedirect.com/science/article/pii/S0927025614002742>.
- [17] V. Sorkin et al. 'First-principles-based high-throughput computation for high entropy alloys with short range order'. In: *Journal of Alloys and Compounds* 882 (2021), p. 160776. ISSN: 0925-8388. DOI: <https://doi.org/10.1016/j.jallcom.2021.160776>. URL: <https://www.sciencedirect.com/science/article/pii/S092583882102185X>.
- [18] Clas Persson. *A Brief Introduction to the Density Functional Theory*. 1st ed. Department of Physics, University of Oslo, 2020.

- [19] David S. Sholl and Janice A. Steckel. 'Density functional theory a practical introduction'. In: (2009).
- [20] Daniel W. Hook, Simon J. Porter and Christian Herzog. 'Dimensions: Building Context for Search and Evaluation'. In: *Frontiers in Research Metrics and Analytics* 3 (2018). <https://www.frontiersin.org/articles/10.3389/frma.2018.00023/pdf>, p. 23. DOI: 10.3389/frma.2018.00023. URL: <https://app.dimensions.ai/details/publication/pub.1106289502>.
- [21] Aron J. Cohen, Paula Mori-Sánchez and Weitao Yang. 'Insights into Current Limitations of Density Functional Theory'. In: *Science* 321.5890 (2008), pp. 792–794. DOI: 10.1126/science.1158722. eprint: <https://www.science.org/doi/pdf/10.1126/science.1158722>. URL: <https://www.science.org/doi/abs/10.1126/science.1158722>.
- [22] John P. Perdew and Mel Levy. 'Physical Content of the Exact Kohn-Sham Orbital Energies: Band Gaps and Derivative Discontinuities'. In: *Phys. Rev. Lett.* 51 (20 Nov. 1983), pp. 1884–1887. DOI: 10.1103/PhysRevLett.51.1884. URL: <https://link.aps.org/doi/10.1103/PhysRevLett.51.1884>.
- [23] Michael Foster and Karl Sohlberg. 'Empirically corrected DFT and semi-empirical methods for non-bonding interactions'. In: *Physical Chemistry Chemical Physics - PHYS CHEM CHEM PHYS* 12 (Jan. 2010). DOI: 10.1039/b912859j.
- [24] Carlos Borca (<https://scicomp.stackexchange.com/users/8020/carlos-borca>). *Limitations of Density Functional Theory as a computational method?* Computational Science Stack Exchange. eprint: <https://scicomp.stackexchange.com/q/11443>. URL: <https://scicomp.stackexchange.com/q/11443>.
- [25] NobelPrize.org. *The Nobel Prize in Chemistry 1998*. Accessed: 2022-15-04. URL: <https://www.nobelprize.org/prizes/chemistry/1998/summary/>.
- [26] John P Perdew and Yue Wang. 'Accurate and simple analytic representation of the electron-gas correlation energy'. In: *Physical review B* 45.23 (1992), p. 13244.
- [27] John P Perdew, Kieron Burke and Matthias Ernzerhof. 'Generalized gradient approximation made simple'. In: *Physical review letters* 77.18 (1996), p. 3865.
- [28] Fabian (<https://mattermodeling.stackexchange.com/users/295/fabian>). *What makes PBE the most preferred functional over other GGA functionals?* Matter Modeling Stack Exchange. URL: <https://mattermodeling.stackexchange.com/q/402>.
- [29] Jianmin Tao et al. 'Climbing the Density Functional Ladder: Nonempirical Meta-Generalized Gradient Approximation Designed for Molecules and Solids'. In: *Phys. Rev. Lett.* 91 (14 Sept. 2003), p. 146401. DOI: 10.1103/PhysRevLett.91.146401. URL: <https://link.aps.org/doi/10.1103/PhysRevLett.91.146401>.

- [30] Fabien Tran and Peter Blaha. 'Importance of the Kinetic Energy Density for Band Gap Calculations in Solids with Density Functional Theory'. In: *The Journal of Physical Chemistry A* 121.17 (2017). PMID: 28402113, pp. 3318–3325. DOI: 10.1021/acs.jpca.7b02882. eprint: <https://doi.org/10.1021/acs.jpca.7b02882>. URL: <https://doi.org/10.1021/acs.jpca.7b02882>.
- [31] Jianwei Sun, Adrienn Ruzsinszky and John P. Perdew. 'Strongly Constrained and Appropriately Normed Semilocal Density Functional'. In: *Phys. Rev. Lett.* 115 (3 July 2015), p. 036402. DOI: 10.1103/PhysRevLett.115.036402. URL: <https://link.aps.org/doi/10.1103/PhysRevLett.115.036402>.
- [32] Jianwei Sun et al. 'Accurate first-principles structures and energies of diversely bonded systems from an efficient density functional'. In: *Nature chemistry* 8.9 (2016), pp. 831–836.
- [33] Arup Chakraborty et al. 'Predicting accurate cathode properties of layered oxide materials using the SCAN meta-GGA density functional'. In: *npj Computational Materials* 4.1 (2018), pp. 1–9.
- [34] Axel D Becke and Erin R Johnson. 'A simple effective potential for exchange'. In: *The Journal of chemical physics* 124.22 (2006), p. 221101.
- [35] Pedro Borlido et al. 'Large-Scale Benchmark of Exchange–Correlation Functionals for the Determination of Electronic Band Gaps of Solids'. In: *Journal of Chemical Theory and Computation* 15.9 (2019). PMID: 31306006, pp. 5069–5079. DOI: 10.1021/acs.jctc.9b00322. eprint: <https://doi.org/10.1021/acs.jctc.9b00322>. URL: <https://doi.org/10.1021/acs.jctc.9b00322>.
- [36] Carlo Adamo and Vincenzo Barone. 'Toward reliable density functional methods without adjustable parameters: The PBE0 model'. In: *The Journal of Chemical Physics* 110.13 (1999), pp. 6158–6170. DOI: 10.1063/1.478522. eprint: <https://doi.org/10.1063/1.478522>. URL: <https://doi.org/10.1063/1.478522>.
- [37] Aliaksandr V. Krukau et al. 'Influence of the exchange screening parameter on the performance of screened hybrid functionals'. In: *The Journal of Chemical Physics* 125.22 (2006), p. 224106. DOI: 10.1063/1.2404663. eprint: <https://doi.org/10.1063/1.2404663>. URL: <https://doi.org/10.1063/1.2404663>.
- [38] Jochen Heyd, Gustavo E Scuseria and Matthias Ernzerhof. 'Hybrid functionals based on a screened Coulomb potential'. In: *The Journal of chemical physics* 118.18 (2003), pp. 8207–8215.
- [39] Paula Mori-Sánchez and Aron J. Cohen. 'The derivative discontinuity of the exchange–correlation functional'. In: *Phys. Chem. Chem. Phys.* 16 (28 2014), pp. 14378–14387. DOI: 10.1039/C4CP01170H. URL: <http://dx.doi.org/10.1039/C4CP01170H>.

- [40] G. Kresse and D. Joubert. 'From ultrasoft pseudopotentials to the projector augmented-wave method'. In: *Phys. Rev. B* 59 (3 Jan. 1999), pp. 1758–1775. DOI: 10.1103/PhysRevB.59.1758. URL: <https://link.aps.org/doi/10.1103/PhysRevB.59.1758>.
- [41] P. E. Blöchl. 'Projector augmented-wave method'. In: *Phys. Rev. B* 50 (24 Dec. 1994), pp. 17953–17979. DOI: 10.1103/PhysRevB.50.17953. URL: <https://link.aps.org/doi/10.1103/PhysRevB.50.17953>.
- [42] Anubhav Jain et al. 'The Materials Project: A materials genome approach to accelerating materials innovation'. In: *APL Materials* 1.1 (2013), p. 011002. ISSN: 2166532X. DOI: 10.1063/1.4812323. URL: <http://link.aip.org/link/AMPADS/v1/i1/p011002/s1%5C&Agg=doi>.
- [43] Peter E. Blöchl, O. Jepsen and O. K. Andersen. 'Improved tetrahedron method for Brillouin-zone integrations'. In: *Phys. Rev. B* 49 (23 June 1994), pp. 16223–16233. DOI: 10.1103/PhysRevB.49.16223. URL: <https://link.aps.org/doi/10.1103/PhysRevB.49.16223>.
- [44] Jürgen Furthmüller. *How might I calculate the exact bandgap from DOSCAR ?* May 2015.